Conceptual Linearization of Euler Governing Equations to Solve High Speed Compressible Flow Using a Pressure-Based Method

Masoud Darbandi,[1] **Ehsan Roohi,**[1] **Vahab Mokarizadeh**[2]
[1] *Department of Aerospace Engineering, Sharif University of Technology, Tehran, P.O. Box 11365-8639, Iran*

[2] *Energy & Environmental Research Center, Niroo Research Institute, Tehran, P.O. Box 14665-517, Iran*

Received 26 February 2006; revision 30 November 2006; accepted 4 May 2007
Published online in Wiley InterScience (www.interscience.wiley.com).
DOI 10.1002/num.20275

The main objective of the current work is to introduce a new conceptual linearization strategy to improve the performance of a primitive shock-capturing pressure-based finite-volume method. To avoid a spurious oscillatory solution in the chosen collocated grids, both the primitive and extended methods utilize two convecting and convected momentum expressions at each cell face. The expressions are obtained via a physical-based discretization of two inclusive statements, which are constructed via a novel incorporation of the continuity and momentum governing equations. These two expressions in turn provide a strong coupling among the Euler conservative statements. Contrary to the primitive work, the linearization in the current work respects the definitions and essence of physics behind deriving the Euler governing equations. The accuracy and efficiency of the new formulation are then investigated by solving the shock tube as a problem with moving normal and expansion waves and the converging-diverging nozzle as a problem with strong stationary normal shock. The results show that there is good improvement in performance of the primitive pressure-based shock-capturing method while its superior accuracy is not deteriorated at all. Numer Methods Partial Differential Eq 00: 000–000, 2007

Keywords: collocated grid; compressible flow; finite volume method; Newton–Raphson linearization scheme; pressure-based approach; shock-capturing technique

I. INTRODUCTION

The key role of density in high speed flow regimes has resulted in choosing it as a major dependent variable in developing numerical algorithms to solve either Euler or Navier–Stokes governing equations. As a preliminary step, the Godunov method was established based on the important role of density changes in high speed flow regimes [1]. Since the innovation, this primitive method has

Correspondence to: M. Darbandi, Department of Aerospace Engineering, Sharif University of Technology, Tehran, P.O. Box 11365-8639, Iran (e-mail: darbandi@sharif.edu)

been widely improved from different perspectives including accuracy, conservativity, stability, and consistency, e.g., see Refs. [2–5]. For example, to capture shock more precisely, the primitive method has been incorporated with high resolution schemes. Moreover, to reduce the complexity in the high resolution formulations, there have been attempts to compact the computational stencil while maintaining the same order of accuracy [6]. Despite such progresses in density-based methods, there is major difficulty to solve low Mach number flows efficiently [7–9]. The difficulty can be overcome using low Mach number preconditioning, which consequently increases the computational cost. Therefore, there has been serious demand to extend new methods capable of solving not only high speed compressible flow but also low Mach number flow with similar efficiencies. In this regard, the pressure-based methods have been practiced to lessen the difficulties encountered in solving low Mach flows. As it is known, pressure performs no deficiency in solving low Mach number flow [10–14]. To benefit from this advantage, Rossow [15] developed an alternative method to low speed preconditioning for the computations of nearly incompressible flows using a blended pressure/density based method. The evolution of the pressure-based methods is described shortly.

From the conservation perspective, the advantages of finite volume method have promoted the computational fluid dynamics workers to employ it widely. There are two basic choices to write the finite volume formulation if a pressure-based algorithm is chosen. One choice is the type of primary dependent variables utilized in the computational algorithm and the other one is the relative locations of the dependent variables on the computational grids. The primitive finite-volume work of Patankar and Spalding [16], which is known as SIMPLE, considers the continuity equation as a constraint equation for pressure. However, SIMPLE and its variants suffer non-physical oscillatory pressure and velocity fields. Staggered grid arrangement has been employed as a general remedy to overcome the drawbacks. This arrangement stores the dependent variables at two different locations, which are displaced with respect to each other [12, 17]. Boundary condition implementation difficulty and excessive book-keeping are two major objections to staggered grid approaches. In addition, the velocities that satisfy mass do not necessarily conserve momentum in the same control volume. Moreover, more smearing is pronounced around discontinuities [13]. These drawbacks become more crucial in the curvilinear coordinate systems to solve either laminar [18, 19] or turbulent [20, 21] flow regimes. Therefore, the geometrically simplicity of the collocated grid arrangement is very attractive and it will be significant if the cause of wavy non-physical pressure field is removed [22].

There are different approaches to suppress the checkerboard problem on a collocated grid. Rhie and Chow [23] used additional momentum-based interpolation to treat the cell face velocities in the continuity equation. Miller and Schmidt [24] showed that the idea of Ref. [23] would predict spurious cell velocities when local variation of pressure departed considerably from linearity. Askoy and Chen [25] similarly employed momentum weighted interpolation approach to suppress the checkerboard problem in a finite-analytic scheme. Rahman et al. [26] modified the approach of Ref. [23] by incorporating a non-pressure gradient source term in the face approximations. Date [27] derived a new pressure correction equation, which in turn required a further correction called smoothy pressure correction. Darbandi and Schneider [28] derived both cell face velocities via incorporating the mass and momentum governing equations. Lien [11] adopted the collocated storage arrangement for all variables and eliminated the checkerboard oscillations by using a pressure-weighted interpolation method, similar to that of Rhie and Chow [23]. As is seen, the above brief literature review indicates that the dual roles of velocity has been long practiced in collocated schemes. These two velocities can be classified as convected and convecting velocities. They are appropriately substituted in the linearized form of the governing equations. The substitution are normally performed only for the active velocity components in the formulations.

However, the linearization procedure of the governing equations may result in several lagged velocities, which need to be treated very cautiously.

As it is known, the SIMPLE algorithm was originally developed for solving incompressible flow. However, there have been major attempts to extend it for compressible flow treatment as well. Darbandi et al. [12, 29–31] have shown that the SIMPLE algorithm can be readily extended to solve compressible thermobuoyant fields performing high density variation with and without employing the Boussinesq assumption. They have also shown that the extended staggered-based grid is capable of solving subsonic Euler flow regimes [14]. In the route of extending incompressible flow algorithms to treat high compressible flow regimes, Van Doormal et al. [32] also extended SIMPLE and its variants to the solution of compressible flows in the staggered grid context. They used a Newton–Raphson linearization strategy [33] to linearize the mass flux in the continuity equation. Their linearization scheme considers active role for both density and velocity in the derived formulations. Karki and Patankar [10] provided a pressure-based algorithm using SIMPLE procedure. They were not able to capture shock precisely in supersonic flow. One of the famous variants of SIMPLE is PISO algorithm, which includes one predictor and two corrector steps [34]. This algorithm and its variants have been successfully utilized for treating high speed compressible flow regimes [35, 36]. As was mentioned, Lien [11] developed a pressure-based algorithm on collocated grid incorporating the basic idea of Ref. [23] in his algorithm. van der Heul et al. [13] extended an improved marker-and-cell scheme to treat flow in both compressible and incompressible flows. Darbandi and Schneider [28] also developed a fully implicit pressure-based algorithm and solved flow at all speeds on a collocated grid arrangement. Contrary to Ref. [23], they considered alternative roles for velocity to suppress the spurious solutions. Additionally, they employed the Newton–Raphson linearization strategy to linearize the nonlinear convection terms in the momentum equations. Since there are dual roles for the two velocity components in the momentum convection terms, the linearization strategy would be constructed in a manner, which maintains the individual role and conceptual meaning of each velocity in the formulation. This is a key point which has not been taken into account in the preceding collocated algorithms.

The major contribution of the current work is to correct the linearization procedure taken in a primitive pressure-based shock-capturing method [37–39] via employing a novel conceptual linearization, which fully respects the essence of physics behind establishing the flow governing equations. This by itself is a contribution and the new scheme does not necessarily need exhibiting a better performance than the primitive method. However, our investigation shows that the efficiency of the extended method is considerably higher than the primitive one while its accuracy is the same as the primitive one. This outcome can be counted as the second contribution of the current work. To present the achieved outcomes, the extended formulation is evaluated against the primitive one by solving the shock tube and converging-diverging nozzle problems. The accuracy and efficiency of the new algorithm are then compared with those of the primitive work.

II. GOVERNING EQUATIONS

In shock-capturing techniques, it is very customary to present the performance of the newly developed methods by treating the steady quasi-1D and unsteady 1D problems. Similar to many past investigators, who have chosen either steady flow in converging-diverging nozzle problem [40–42] or unsteady flow in shock tube problem [5, 13, 43], we choose the unsteady quasi-1D governing equations to quantify the performance of our proposed linearization. We have targeted

both the steady quasi-1D flow and the unsteady Riemann problems in our study. The unsteady quasi-one-dimensional form of the Euler governing equations is written as

$$\frac{\partial \mathbf{q}}{\partial \tau} + \frac{\partial \mathbf{B}(\mathbf{q})}{\partial x} = \mathbf{s} \tag{2.1}$$

where the solution vector $\mathbf{q}$, the convection flux vector $\mathbf{B}(\mathbf{q})$, and the source term vector $\mathbf{s}$ are respectively given by

$$\mathbf{q} = (\rho A,\ \rho u A,\ \rho e A)^T \tag{2.2}$$

$$\mathbf{B} = (\rho u A,\ \rho u^2 A,\ \rho u e A + p u A)^T \tag{2.3}$$

$$\mathbf{s} = (0,\ -A(\partial p/\partial x), 0)^T \tag{2.4}$$

In the earlier equations, τ, ρ, p, u, and A represent time, density, pressure, velocity, and the cross-section area, respectively. If we neglect the change in potential energy, the total energy per unit mass for a perfect gas is given by $e = c_v t + u^2/2$, where t is temperature and c_v is the specific heat value at constant volume. Considering this expression, the equation of state $p = \rho R t$ relates the velocity and pressure fields to the temperature field in compressible flows. The discretized governing equations are simultaneously solved for pressure p, temperature t, and momentum component $f(\equiv \rho u)$ variables of which the latter one is chosen instead of the velocity variable. Past experience has shown that the use of momentum component as a dependent variable can result in several important outcomes in a pressure-based shock-capturing method. For example, it provides a strong analogy between the compressible and incompressible governing equations. This in turn enables the solution of compressible flow using incompressible methods [12, 37]. It simplifies the required linearization procedure [38]. It suppresses the oscillations occurred passing through a discontinuity [44]. It can also improves the performance of the pressure-based shock-capturing methods [39].

III. DOMAIN DISCRETIZATION

Figure 1 illustrates the grid distribution in a converging-diverging nozzle. The control volumes are located between the crosses, which are called integration points. The grid nodes are located at the geometric centers of control volumes. They are shown by circles. The subscripts E and W are used to denote the nodal quantities associated with the control volume to the east and west of the control volume centered at node P. Similarly, e and w indicate the east and west faces of the same control volume. In this study, upper case letters such as P, U, T, and ϱ are associated with

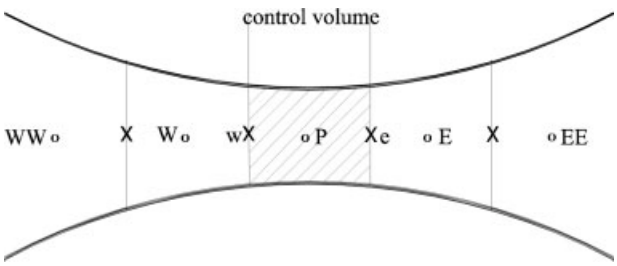

FIG. 1. The nomenclature used for the cell faces and their neighboring cells.

quantities at main nodes, while lower case letters such as p, u, t, and ρ refer to quantities at the cell faces (or integration points).

IV. COMPUTATIONAL MODELLING

Equation (2.1) can be integrated over an arbitrary control volume, see the shaded volume in Fig. 1. Using the divergence theorem, integration of the continuity equation yields

$$\iint_A \frac{\partial(\rho A)}{\partial \tau} dA + \int_S (\rho u A) dS = 0 \tag{4.1}$$

where S indicates the integration over the cell faces. Since the current method is fully implicit, the second term is evaluated at the advanced time and the transient term is approximated using a mass-lumped approach. The latter treatment yields

$$\iint_A \frac{\partial(\rho A)}{\partial \tau} dA \approx \Delta x \frac{(\varrho_{\mathrm{P}} - \varrho_{\mathrm{P}}^o)}{\Delta \tau} A_{\mathrm{P}} \tag{4.2}$$

where ϱ_{P}^o indicates the lumped density of the cell centered at P and its magnitude is obtained from the preceding time step. The second term in Eq. (4.1) is simply integrated over the boundary of the cell. It results in

$$\int_S (\rho u A) dS \approx (\rho u A)_{\mathrm{e}} - (\rho u A)_{\mathrm{w}} \tag{4.3}$$

Eventually, the discretized form of the mass equation can be written as

$$\frac{\Delta x(\varrho_{\mathrm{P}} - \varrho_{\mathrm{P}}^o)}{\Delta \tau} + j_{\mathrm{e}}(\rho u)_{\mathrm{e}} - j_{\mathrm{w}}(\rho u)_{\mathrm{w}} = 0 \tag{4.4}$$

The parameters $j_{\mathrm{e}} = A_{\mathrm{e}}/A_{\mathrm{P}}$ and $j_{\mathrm{w}} = A_{\mathrm{w}}/A_{\mathrm{P}}$ represent the ratios of the east and west cell face areas respectively to the area at the cell center. Since density is considered as a secondary unknown in our pressure-based algorithm, the transient term in Eq. (4.4) needs to be linearized further. A simple linearization idea is suggested as $\varrho = (1/R\bar{T})P$, which considers an active role for P and a passive role for T. Alternatively, we may employ a Taylor series of that to consider active roles for both P and T, i.e.,

$$\varrho \approx \bar{\varrho} + \overline{\frac{\partial \varrho}{\partial P}}(P - \bar{P}) + \overline{\frac{\partial \varrho}{\partial T}}(T - \bar{T}) \tag{4.5}$$

where

$$\overline{\frac{\partial \varrho}{\partial P}} = \frac{1}{R\bar{T}} \quad \overline{\frac{\partial \varrho}{\partial T}} = -\frac{\bar{P}}{R\bar{T}^2} \tag{4.6}$$

The integration of the momentum equation over the chosen control volume yields

$$\iint_A \frac{\partial(\rho u A)}{\partial \tau}\, dA + \int_S (\rho u^2 A)\, dS + \iint_A \left[\frac{\partial(pA)}{\partial x} - p\frac{\partial A}{\partial x}\right] dA = 0 \tag{4.7}$$

The use of a mass-lumped approach for the transient term results in

$$\iint_A \frac{\partial(\rho u A)}{\partial \tau}\, dA \approx \frac{\Delta x[(\varrho U)_P - (\varrho U)_P^o]}{\Delta \tau} A_P \tag{4.8}$$

Additionally, the integration of the momentum convection term over the cell faces yields

$$\int_S (\rho u^2 A)\, dS \approx (\rho u^2 A)_{\mathrm{e}} - (\rho u^2 A)_{\mathrm{w}} \tag{4.9}$$

The last term in Eq. (4.7) can be approximated by

$$\iint_A \left[\frac{\partial (pA)}{\partial x} - p \frac{\partial A}{\partial x} \right] dA \approx (pA)_{\mathrm{e}} - (pA)_{\mathrm{w}} - P_{\mathrm{p}}(A_{\mathrm{e}} - A_{\mathrm{w}}) \tag{4.10}$$

Eventually, the discretized form of the momentum equation can be presented by

$$\frac{\Delta x[(\varrho U)_{\mathrm{P}} - (\varrho U)^o_{\mathrm{P}}]}{\Delta \tau} + j_{\mathrm{e}} u_{\mathrm{e}} (\rho u)_{\mathrm{e}} - j_{\mathrm{w}} u_{\mathrm{w}} (\rho u)_{\mathrm{w}} + j_{\mathrm{e}}\, p_{\mathrm{e}} - j_{\mathrm{w}}\, p_{\mathrm{w}} - P_{\mathrm{P}}(j_{\mathrm{e}} - j_{\mathrm{w}}) = 0 \tag{4.11}$$

To be able to use a linear algebraic solver in our fully implicit algorithm, the nonlinear convection terms in Eq. (4.11) need to be linearized properly. Assuming the momentum component ρu as a primary dependent variable, a simple linearization scheme suggests

$$\rho u u \approx \bar{u}(\rho u) \tag{4.12}$$

However, a more sophisticated linearization, which considers the active impact of the two variables, is obtained using the Newton–Raphson Linearization Scheme, NRLS [33]. The use of NRLS results in

$$u(\rho u) \approx \bar{u}(\rho u) + (\overline{\rho u})u - \overline{\rho u u} \tag{4.13}$$

If NRLS is further applied to $u = \rho u/\rho$ in the second term on the RHS, Eq. (4.13) becomes

$$\rho u u \approx 2\bar{u}(\rho u) - \bar{u}^2 \rho \tag{4.14}$$

A general expression to include both Eqs. (4.12) and (4.14) can be defined as

$$\rho u u \approx 2k_1 \bar{u}(\rho u) - k_2 \bar{u}^2 \rho \tag{4.15}$$

where k_1 and k_2 are two constants. If $k_1 = k_2 = 1$, it results in NRLS, i.e., Eq. (4.14). On the other hand, if $k_1 = 1/2$ and $k_2 = 0$, it yields a simple linearization, i.e., Eq. (4.12). Equation (4.14) has been tested in 1D investigation with success [38, 45]. The experience has shown that NRLS would generally perform better than the simple linearization scheme.

The next step is to treat the energy equation. This equation involves more nonlinear terms than the preceding equations. The energy equation can be similarly integrated over the chosen control volume. It yields

$$\iint_A \frac{\partial (\rho e A)}{\partial \tau} dA + \int_S A(\rho u e + p u)\, dS = 0 \tag{4.16}$$

Similar to the mass and momentum equations, the integrals can be treated properly. The conservable form can be eventually written as

$$\frac{\Delta x[(\varrho\, E)_{\mathrm{P}} - (\varrho\, E)^o_{\mathrm{P}}]}{\Delta \tau} + (\rho u e j)_{\mathrm{e}} - (\rho u e j)_{\mathrm{w}} + (p u j)_{\mathrm{e}} - (p u j)_{\mathrm{w}} = 0 \tag{4.17}$$

The nonlinear ϱE in the transient term can be linearized with respect to ϱ and E using NRLS. On the other hand, the internal energy variable E can be linearized to $E = c_v T + (\bar{U}/2\bar{\varrho})(\varrho U)$. Our experience shows that these linearizations provide more robust convergence. Using these linearization strategies, the transient term in Eq. (4.17) is approximated by

$$\frac{\Delta x[(\varrho E)_{\mathrm{P}} - (\varrho E)_{\mathrm{P}}^{o}]}{\Delta\tau} \approx \frac{\Delta x}{\Delta\tau}\left[\frac{\bar{U}}{2}(\varrho U) + \frac{\bar{E}}{R\bar{T}}P + \left(\bar{\varrho}c_v - \frac{(\bar{\varrho}\bar{E})}{\bar{T}}\right)T - (\varrho E)^{o}\right]_{\mathrm{P}} \tag{4.18}$$

Similarly, using NRLS for ρue term, linearizing it with respect to e and ρu, and utilizing the linearized form suggested for E (or e) finally yield

$$\rho ue \approx \left(\bar{e} + \frac{\bar{u}^2}{2}\right)f + (c_v\overline{f})t - (\overline{ef}) \tag{4.19}$$

The two last terms in the LHS of Eq. (4.17) can be converted to Rtf. This can be achieved via the equation of state. Additionally, Rtf can be linearized with respect to f and t using either simple linearization or NRLS. The latter choice results in

$$up = Rtf \approx (c_{\mathrm{p}} - cv)(\bar{t}f - \bar{f}t) - R\overline{ft} \tag{4.20}$$

The combination of Eqs. (4.19) and (4.20) is given by

$$\rho ue + up \approx (c_{\mathrm{p}}\bar{t} + \overline{u}^2)f + (c_{\mathrm{p}}\bar{f})t - (\bar{e} + R\bar{t})\bar{f} \tag{4.21}$$

The substitutions of Eqs. (4.18) and (4.21) in Eq. (4.17), the discretized energy equation is written as

$$\frac{\Delta x}{\Delta\tau}\left[\frac{\bar{U}}{2}(\varrho U) + \frac{\bar{E}}{R\bar{T}}P + \left(\bar{\varrho}c_{\mathrm{v}} - \frac{(\bar{\varrho}\bar{E})}{\bar{T}}\right)T - (\varrho E)^{o}\right]_{\mathrm{P}} + [(c_{\mathrm{p}}\bar{t} + \overline{u}^2)f + (c_{\mathrm{p}}\bar{f})t - (\bar{e} + R\bar{t})\bar{f}]j_e$$
$$- \{[(c_{\mathrm{p}}\bar{t} + \overline{u}^2)f + (c_{\mathrm{p}}\bar{f})t - (\bar{e} + R\bar{t})\bar{f}]j\}_{\mathrm{w}} = 0 \tag{4.22}$$

By this derivation, the discretization of the Euler governing equation is finished. The next step is to approximate the magnitudes at cell faces in terms of the magnitudes at the nodes. At this stage, it is worth to mention that there are many different choices to linearize the nonlinear terms in the conservative statements. However, our main objective in this work is not to examine the impact of different possible linearizations but to extend our conceptual linearization, which is applicable to nonlinear convection terms in the momentum equations, see Section C.

A. Integration Point Equations

To make the algebraic system of equations well-posed, this stage of our modelling requires to present the major dependent variables at cell faces in terms of nodal variables, see f (or ρu) in Eq. (4.4), p in Eq. (4.11), and t in Eq. (4.22). Therefore, it is necessary to derive suitable expressions for momentum component, pressure, and temperature at the cell faces. Upwind, QUICK, and HYBRID schemes can be nominated as suitable mathematical interpolations [17]. Alternatively, there are more advanced schemes, which include more physics of flow. For example, Prakash and Patankar [46] presented profiles which were attempting to include the relevant physics into the interpolation functions. Schneider and Raw [47] employed Physical Influence Scheme PIS, which

considered the flow governing equations, to derive the integration point expressions in incompressible flow simulations. Darbandi and Schneider [28, 37] extended this model to compressible flow simulations. The fundamental concepts of PIS will be employed in this work as well.

The expressions for the momentum components can be derived from the momentum equation. In this regard, the momentum equation given in Eq. (2.1) is expanded to

$$A\frac{\partial f}{\partial \tau}+u\frac{\partial (fA)}{\partial x}+fA\frac{\partial u}{\partial x}+A\frac{\partial p}{\partial x}=0 \tag{4.23}$$

The terms in this equation are differenced in certain manners, which respect the correct physics of flow. To achieve this purpose, they are approximated by

$$A\frac{\partial f}{\partial \tau}\bigg|_{\mathrm{e}}\approx A_{\mathrm{e}}\frac{f_{\mathrm{e}}-f_{\mathrm{e}}^{o}}{\Delta \tau} \tag{4.24}$$

$$u\frac{\partial (fA)}{\partial x}\bigg|_{\mathrm{e}}\approx \overline{u}_{\mathrm{e}}\frac{(Af)_{\mathrm{e}}-(AF)_{\mathrm{P}}}{\Delta x/2} \tag{4.25}$$

$$fA\frac{\partial u}{\partial x}\bigg|_{\mathrm{e}}\approx \frac{\overline{f}_{\mathrm{e}}A_{\mathrm{e}}(f_{\mathrm{e}}/\bar{\rho}_{\mathrm{e}}-F_{\mathrm{P}}/\bar{\varrho}_{\mathrm{P}})}{\Delta x/2} \tag{4.26}$$

$$A\frac{\partial p}{\partial x}\bigg|_{\mathrm{e}}\approx A_{\mathrm{e}}\frac{P_{\mathrm{E}}-P_{\mathrm{P}}}{\Delta x} \tag{4.27}$$

Consistent with their physics, the convection terms are treated in an upwind manner. Another possible form for Eq. (4.26) is $fA\partial u/\partial x \approx A\overline{\partial u/\partial x}\ f$. However, this scheme resulted in poor convergence of the method. The substitutions of the discretized terms into Eq. (4.23) and its rearrangement finally result in an expression for the momentum component at integration point. A compact form of that can be written as

$$f_{\mathrm{e}}=\frac{2C_{\mathrm{e}}(A_{\mathrm{P}}/A_{\mathrm{e}}+\bar{\rho}_{\mathrm{e}}/\bar{\varrho}_{\mathrm{P}})}{1+4C_{\mathrm{e}}}F_{\mathrm{P}}+\frac{C_{\mathrm{e}}}{\bar{u}_{\mathrm{e}}(1+4C_{\mathrm{e}})}(P_P-P_E)+\frac{f_{\mathrm{e}}^{o}}{1+4C_{\mathrm{e}}} \tag{4.28}$$

where the Courant number is defined as $C=\bar{u}\,\Delta t/\Delta x$. Equation (4.28) indicates that the use of a physical influence scheme produces a strong connection between the integration point variable at face e and its neighboring nodal variables located at P and E. It can be shown that the substitutions of f_{e} and f_{w} in the mass Eq. (4.4) and momentum Eq. (4.11) equations provide reliable coupling between pressure and velocity fields.

The expression for the temperature at integration point can be obtained by suitable discretization of the energy equation given by Eq. (2.1). This equation is rewritten as

$$\rho c_{\mathrm{v}}\frac{\partial t}{\partial \tau}+\rho u c_{\mathrm{v}}\frac{\partial t}{\partial x}+p\frac{\partial u}{\partial x}+pu\frac{\partial [\ln(A)]}{\partial x}=0 \tag{4.29}$$

The transient term is discretized similar to Eq. (4.24). The upwind and central differences are utilized for the second and third terms, respectively. The last term is treated as a source term.

These considerations yield

$$\rho c_{\mathrm{v}} \frac{\partial t}{\partial \tau}\bigg|_{\mathrm{e}} \approx \bar{\rho}_{\mathrm{e}} c_{\mathrm{v}} \frac{t_{\mathrm{e}} - t_{\mathrm{e}}^{o}}{\Delta \tau} \tag{4.30}$$

$$\rho u c_{\mathrm{v}} \frac{\partial t}{\partial x}\bigg|_{\mathrm{e}} \approx \bar{f}_{\mathrm{e}} c_{\mathrm{v}} \frac{t_{\mathrm{e}} - T_{\mathrm{P}}}{\Delta x/2} \tag{4.31}$$

$$p \frac{\partial u}{\partial x}\bigg|_{\mathrm{e}} \approx \bar{p}_{\mathrm{e}} \frac{U_{\mathrm{E}} - U_{\mathrm{P}}}{\Delta x} \tag{4.32}$$

$$pu \frac{\partial [\ln(A)]}{\partial x}\bigg|_{\mathrm{e}} \approx \bar{p}_{\mathrm{e}} \bar{u}_{\mathrm{e}} \frac{\partial [\ln(A)]}{\partial x}\bigg|_{\mathrm{e}} \tag{4.33}$$

Using the earlier approximations, the temperature expression at integration point is obtained from

$$t_{\mathrm{e}} \approx \frac{2C_{\mathrm{e}}}{(1+2C_{\mathrm{e}})} T_{\mathrm{p}} + \frac{C_{\mathrm{e}} \bar{p}_{\mathrm{e}}}{(\bar{\rho}\bar{u})_{\mathrm{e}} c_{\mathrm{v}} (1+2C_{\mathrm{e}})} \left(\frac{F_{\mathrm{P}}}{\bar{\varrho}_{\mathrm{P}}} - \frac{F_{\mathrm{E}}}{\bar{\varrho}_{\mathrm{E}}} \right) - \frac{\Delta x C_{\mathrm{e}} \bar{p}_{\mathrm{e}}}{\bar{\rho}_{\mathrm{e}} c_{\mathrm{v}} (1+2C_{\mathrm{e}})} \frac{\partial [\ln(A)]}{\partial x}\bigg|_{\mathrm{e}} + \frac{t_{\mathrm{e}}^{o}}{(1+2C_{\mathrm{e}})} \tag{4.34}$$

Furthermore, the unknown density at integration points can be calculated from the equation of state. In this regard, the equation of state can be firstly linearized with respect to pressure and temperature using Eq. (4.5). Secondly, the pressure (see the next paragraph) and temperature, Eq. (4.34), expressions are substituted in that.

Schneider and Raw [47] used the pressure Poisson equation as an explicit equation and showed that the pressure field would be strongly elliptic in incompressible flow. Similarly, we use a linear interpolation to determine the pressure variable at integration points, i.e., $p_{\mathrm{e}} \approx (P_{\mathrm{P}} + P_{\mathrm{E}})/2$, if the local flow is subsonic. However, if the flow is supersonic we utilize an upwind scheme to approximate the pressure at the cell faces.

B. Checkerboard Problem and Remedy

In the preceding section, we obtained f, p, t, and ρ expressions at the cell faces. The substitution of these expressions in Eqs. (4.4, 4.11, 4.22) eliminates the unknowns at the cell faces in our derivations. However, it is necessary to investigate the checkerboard problem in our extended collocated formulation. Darbandi and Bostandoost [44] launched their incompressible investigation and showed that the substitution of the derived momentum expression, Eq. (4.28), in both mass Eq. (4.4) and momentum Eq. (4.11) equations might produce unrealistic wavy pressure and momentum solutions. Unfortunately, the spurious solutions fully satisfy the governing equations and their imposed boundary conditions. This instability in the solution is similarly reported by other finite-volume pressure-based investigators [22]. To suppress such non-physical zigzag solutions, they suggest and employ a new statement to derive the second expression for the momentum component at the integration point. Their primary purpose has been to include the role of continuity equation in deriving the second momentum component expression. Thus, the second expression should be obtained in a manner, which takes into account the roles of not only the mass but also the momentum governing equations. To achieve their purpose, they suggested

$$[(\text{Momentum Eq. Error}) - u(\text{Mass Eq. Error})] = 0 \tag{4.35}$$

As is seen, this suggestion takes into account the effect of both continuity and momentum equation errors in the new expression. The justification behind defining and using this special form is to provide an inclusive statement, very similar to Eq. (4.28), to approximate our second momentum components at the cell faces. To achieve this, we need starting from the basic governing equations, very similar to the one given by Eq. (4.23). In this regard, we suggest a new relation, which is more meaningful for the compressible flow applications. The new relation is defined as

$$\left[A\frac{\partial f}{\partial \tau}+u\frac{\partial (fA)}{\partial x}+fA\frac{\partial u}{\partial x}+A\frac{\partial p}{\partial x}\right]-u\left[A\frac{\partial \rho}{\partial \tau}+\frac{\partial (fA)}{\partial x}\right]=0 \tag{4.36}$$

The above statement indicates that two types of errors are incorporated in extending the second cell-face expression. In fact, if a nonexact solution is substituted into the mass and momentum equations, it will result in errors or residuals for both of them. Additionally, if the nonexact solution does not satisfy only the mass equation, the impact is subsequently appeared in the second cell face expression but not the first one. The discretization of the first brackets in Eq. (4.36) is exactly similar to what was fulfilled for the momentum integration point equation, see Eqs. (4.24)–(4.27). However, the terms in the second brackets are approximated using

$$uA\frac{\partial \rho}{\partial \tau}\bigg|_{\mathrm{e}} \approx \bar{u}_{\mathrm{e}}A_{\mathrm{e}}\left.\frac{\partial \bar{\rho}}{\partial \tau}\right|_{\mathrm{e}} \tag{4.37}$$

$$u\frac{\partial (fA)}{\partial x}\bigg|_{\mathrm{e}} \approx \bar{u}_{\mathrm{e}}\frac{A_{\mathrm{e}}\,f_{\mathrm{e}}-A_{\mathrm{P}}\,F_{\mathrm{P}}}{\Delta x/2} \tag{4.38}$$

The substitutions of Eqs. (4.24)–(4.27) and Eqs. (4.37)–(4.38) in Eq. (4.36) and its suitable rearrangement finally yield

$$\hat{f}_{\mathrm{e}}=\frac{2C_{\mathrm{e}}}{1+2C_{\mathrm{e}}}\frac{\bar{\rho}_{\mathrm{e}}}{\bar{\varrho}_P}F_{\mathrm{p}}+\frac{C_{\mathrm{e}}}{1+2C_{\mathrm{e}}}(P_{\mathrm{P}}-P_{\mathrm{E}})+\frac{f_{\mathrm{e}}^{o}}{1+2C_{\mathrm{e}}}+\frac{C_{\mathrm{e}}\Delta x}{1+2C_{\mathrm{e}}}\left.\frac{\partial \bar{\rho}}{\partial \tau}\right|_{\mathrm{e}} \tag{4.39}$$

We call this new expression convecting momentum and refer to the preceding expression given in Eq. (4.28) as convected momentum. We have labelled the convecting momentum with a hat to distinguish it from the convected one. The substitution of the convecting momentum into the continuity equation Eq. (4.4) entirely suppresses the possibility of a zigzag pressure field in the domain [44]. Moreover, Eq. (4.4) is used to solve the pressure field now. In another words, although the continuity equation in its original form has no trace of active pressure variable, the substitution of Eq. (4.39) in Eq. (4.4) permits to solve Eq. (4.4) for the pressure field now.

C. Conceptual Linearization Strategy

Figure 2 shows an infinitesimal volume with a finite length of δx taken from Fig. 1. The inlet and outlet mass flow rates in addition to their resulting momentum forces are indicated at the left and right faces of the element. Since we are concerned on the role of mass flux, we avoid presenting the pressure forces around this volume. To emphasize the critical role of momentum component in the continuity equation (and subsequently in our formulations), we have used mass flux component f instead of the multiplication of ρ and u, i.e., ρu, in this figure. As it is known,

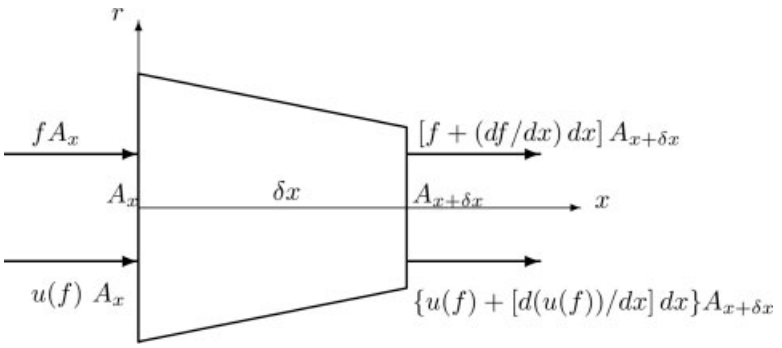

FIG. 2. An infinitesimal element illustrating the inlet and outlet mass fluxes and their resulting momentum forces.

the flow of mass f through the cell face results in momentum on that face, i.e., $u\,(f)$. Considering this point, the balances of mass and momentum for the steady conditions become

$$d(fA)/dx = 0 \tag{4.40}$$

$$d[u(fA)]/dx + A(dp/dx) = 0 \tag{4.41}$$

The f component in these two equations can be replaced with ρu. However, to retain the original role of u in the mass flux component, we identify it with a hat. Therefore, the preceding coupled equations are upgraded to

$$d(\rho\hat{u}A)/dx = 0 \tag{4.42}$$

$$d[u(\rho\hat{u}A)]/dx + A(dp/dx) = 0 \tag{4.43}$$

These two equations contain two velocity components, i.e., u and $\hat{u}$. The velocity component which appears in the mass flux components is named convecting velocity or mass conserving velocity. This name indicates the specific role of the velocity component in mass balance equations, i.e., Eq. (4.40) [or Eq. (4.42)]. On the other hand, the component of u in Eq. (4.41) [or Eq. (4.43)] is called the convected velocity. This velocity convects the mass flux (or transports the scalars) through the control volume. To distinguish these two velocities from each other, the convecting component has been already identified by a hat. The density in the convection term of the momentum equation Eq. (4.43) can be coupled with u instead of $\hat{u}$ without jeopardizing the individual meaning of the convected and convecting velocities. The aforementioned displacement results in

$$d(\rho\hat{u}A)/dx = 0 \tag{4.44}$$

$$d[\hat{u}(\rho uA)]/dx + A(dp/dx) = 0 \tag{4.45}$$

With this knowledge, we can simply define our convected f and convecting $\hat{f}$ momentum components and revise Eqs. (4.44)–(4.45) to

$$d(\hat{f}A)/dx = 0 \tag{4.46}$$

$$d[\hat{u}(fA)]/dx + A(dp/dx) = 0 \tag{4.47}$$

It is worth to note that an arbitrary switch from the convected component to convecting one or vice versa may jeopardize the original concepts on which the governing equations are founded. Additionally, as was mentioned before, the past researchers have shown that the use of two different velocities in the continuity and momentum equations has the advantages of suppressing the possible pressure-velocity decoupling phenomenon in collocated solution domains [23].

Considering the above physical-based definitions, there are two major choices to linearize the convection term in the momentum equation Eq. (4.11) with respect to the momentum component. A simple linearization choice for the convection terms of the momentum equation permits an active role only for the convected momentum component. This linearization scheme results in

$$\hat{u} f \approx \bar{\hat{u}} f \tag{4.48}$$

A second linearization choice is to employ a Newton–Raphson Linearization Scheme (NRLS). This scheme considers more active role for the individual components in the nonlinear term. Back to Eq. (4.13), the convection term in Eq. (4.47) can be linearized to

$$\hat{u}(fA) \approx (\bar{\hat{u}} A) f + (\bar{f} A)\hat{u} - \overline{\hat{u} f} A \tag{4.49}$$

Since $\hat{u}$ is not a major unknown in this study, we use NRLS and linearize the convecting velocity component shown in the second term on the LHS in terms of $(\rho\hat{u})$, i.e.,

$$\hat{u} = \frac{(\rho\hat{u})}{\rho} \approx \frac{1}{\bar{\rho}}(\rho\hat{u}) - \frac{\bar{\hat{u}}}{\bar{\rho}}\rho + \bar{\hat{u}} \tag{4.50}$$

The substitution of Eq. (4.50) in Eq. (4.49) and performing some more simplifications finally result in

$$\hat{u} f \approx \bar{\hat{u}}(f) + \bar{u}(\hat{f}) - \overline{u\hat{u}}\rho \tag{4.51}$$

This linearization scheme considers active roles for both convected and convecting momentum components as well as density in the convection term in Eq. (4.11). The density term may be simply lagged and replaced with the known density of the previous iteration. We leave it in the rest of our formulations as it is. Considering the two definitions of the momentum components, we present a general expression which includes both the simple Eq. (4.48) and NRLS Eq. (4.51) cases. The general form is suggested as

$$\hat{u} f \approx \bar{\hat{u}} f + k'(\bar{u}\hat{f} - \overline{u\hat{u}}\rho) \tag{4.52}$$

where $k' = 0$ results in a simple linearization, i.e., Eq. (4.48), and $k' = 1$ represents NRLS, i.e., Eq. (4.51). If we ignore the individual concepts involved in the convected and convecting components, it yields $\hat{u} = u$ and $\hat{f} = f$. Then, Eq. (4.52) can be replaced with a new one given by

$$(\rho u\, u = \rho\hat{u}\hat{u}) \approx [(2k_1\, \bar{u} f - k_2\, \bar{u}^2\rho) = (2k_1\, \bar{\hat{u}} f - k_2\, \bar{\hat{u}}^2\rho)] \tag{4.53}$$

where k_1 and k_2 are two constants, which make the two linearizations possible. Equation (4.53) is identical with Eq. (4.15), which was derived without the knowledge of convecting and convected components. Similar to Eq. (4.15), the consideration of $k_1 = k_2 = 1$ results in NRLS, i.e., Eq. (4.14), and the consideration of $k_1 = \frac{1}{2}$ and $k_2 = 0$ results in a simple linearization, i.e., Eq. (4.12).

In the following section, we evaluate the performance of our new developed linearizations in solving unsteady and steady flows using either Eq. (4.53) as Simple Newton–Raphson Linearization Scheme (SNRL) or Eq. (4.52) as Improved Newton–Raphson Linearization Scheme (INRL) to linearize the convection terms in the momentum equations, i.e., Eq. (4.11).

V. RESULTS AND DISCUSSION

In this section, the conceptual linearization is applied to solve both steady and unsteady flows with shock. In this regard, the converging-diverging nozzle and shock tube problems are chosen to evaluate the extended formulations. The nozzle problem is known as a standard test case to examine the performance of steady shock-capturing techniques in solving a solution domain with a wide range of Mach numbers including a strong normal shock. Alternatively, the shock tube problem is known as a standard test case to evaluate the unsteady shock-capturing techniques. Both the transient flow features (i.e., moving normal shock and expansion waves as well as a contact discontinuity) and a wide range of flow Mach numbers (i.e., subsonic, transonic, and supersonic regimes) can be targeted in the latter case. To stop the iterations in each time step, the convergence criterion ϵ at each time step is checked using

$$\max(|(P_i - \bar{P}_i)/P_i|,\ |(T_i - \bar{T}_i)/T_i|) \ \leq\ (\epsilon = 10^{-10}) \tag{5.1}$$

where the subscript i represents the node number. The gas properties are $c_v = 720$ J/KgK, $R = 287.0$ J/KgK, and $\gamma = 1.4$.

A. The Accuracy of the Extended Scheme

At the first stage, we examine the unsteady shock tube problem. The shock tube length is 1 m and a total of 201 nodes is uniformly distributed along it. The air pressures are 1,000 and 100 KPa in the high and low-pressure sides, respectively. The initial temperature is 25°C in both sides. Following Refs. [38, 45], the results are normally presented at 500 μs after rupturing the separating diaphragm. Figure 3 illustrates the distributions of density, pressure, temperature, and Mach number using a Courant number of 0.286. The density, pressure, and temperature are nondimensionalized using their respective values in the lower pressure side. The figure presents the

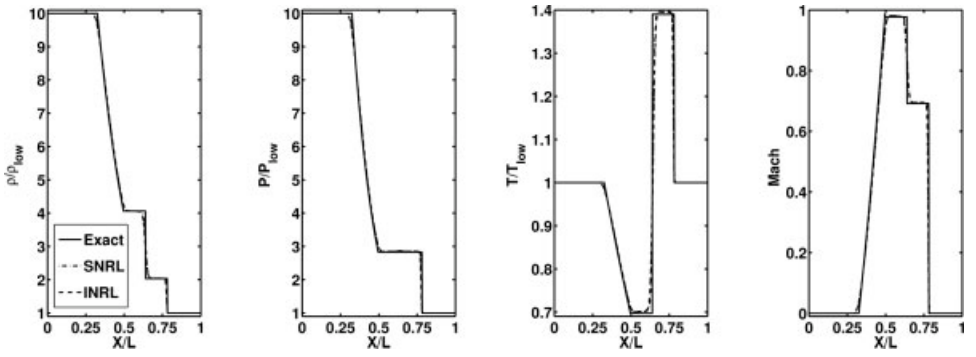

FIG. 3. The numerical solutions in the shock tube problem using both SNRL and INRL schemes and their comparisons with the exact solutions.

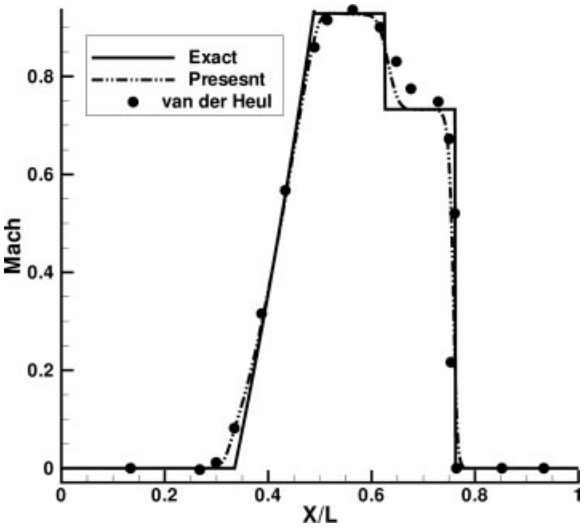

FIG. 4. A comparison of the present solution with that of van der Heul et al. [13].

results of both INRL and SNRL schemes. They are compared with each other and those of analytical solutions. The results of both INRL and SNRL schemes are in good agreement with the analytical solutions. Additionally, the two INRL and SNRL schemes perform similar accuracies. In another words, the numerical solutions are independent of the selected linearization scheme. This conclusion was definitely predictable because the final results of the two schemes should not be significantly affected by the choice of scheme to treat the nonlinear convection terms in the momentum equations.

Although it is not a main concern in this work, our study shows that the accuracy achieved in this unsteady solution is comparable and even better than the accuracies presented by a few other Euler flow solvers. For example, comparing the current results with those of the primitive Godunov method [1], the artificially upstream flux vector splitting of Sun and Takayama [48], and different weighted essentially nonoscillatory schemes of Titarev and Toro [49], the accuracy of the current solution is excellent. It should be noted that the current accuracy is obtained without enforcing any additional filters and/or features. Since it is more rational to compare our results with those of pressure-based methods, Fig. 4 presents the current Mach distribution and compares it with that of van der Heul et al. [13], who benefit from the advantages of a pressure-correction method. They solve Sod's Riemann problem using a few different schemes of which we have chosen the one, which is more consistent with our formulation and its discretization. The Sod's Riemann problem is solved in similar conditions for both cases.

In the next stage, we study the converging-diverging nozzle problem. The nozzle profile is defined as $\text{Area}(x) = 1 + m(x - l/2)^2$, where m is a positive integer and l represents the nozzle length. This equation provides symmetric profiles with respect to the nozzle throat. Depending on the flow conditions at the inlet and outlet, different boundary conditions are required to be employed at the boundaries. For the status with subsonic at the inlet, subsonic at the outlet, and a normal shock wave standing in the divergent part of the nozzle, the pressure, velocity, and temperature are specified at the inlet and the pressure is specified at the outlet. In fact, the back pressure determines the shock position and its strength in the divergent part. Figures 5 and 6 illustrate the distributions of density, pressure, temperature, and Mach number in the nozzle using two back

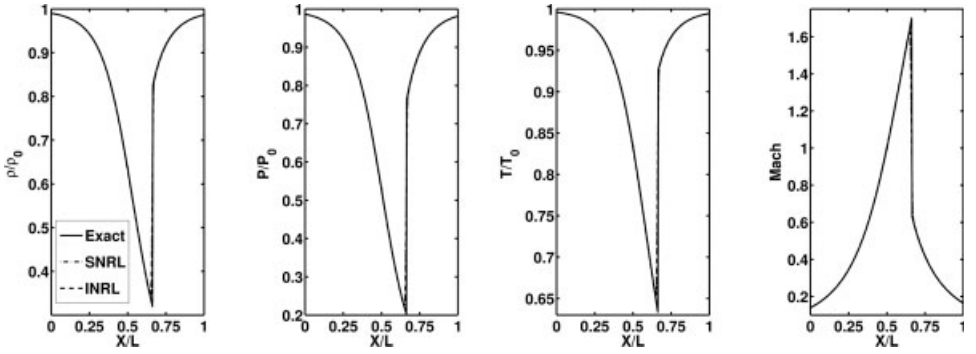

FIG. 5. The present results in a nozzle with $P_b = 85$ kPa using INRL and SNRL schemes and comparing them with the exact solutions.

pressures of 85 and 45 kPa, respectively. The results were obtained using a Courant number of 0.20. Since the velocity magnitude changes throughout the nozzle, the Courant number is calculated based on the maximum velocity occurred within the nozzle, i.e., $C = U_{\max}\Delta t/\Delta x$. The density, pressure, and temperature parameters are non-dimensionalized with respect to their local stagnation point magnitudes. Similar to the shock tube problem, the two INRL and SNRL schemes exhibit similar accuracies and provide excellent agreements with that of the exact solution. Indeed, a stronger shock does not deteriorate the achieved accuracy at all.

To quantify the accuracy of our results, Fig. 7 presents both the mesh refinement study and a comparison with other solutions. Figure 7(a) illustrates the current Mach distributions for the mesh with 80, 160, and 320 resolutions. This plot demonstrates that the mesh with 160 nodes is fine enough to provide reliable accuracy. Therefore, this mesh resolution is chosen to validate our results against the exact solution and the solution provided by Rossow [42], see Fig. 7(b). To have a fair comparison, we have presented the results of Rossow for a similar grid distribution. Similar to our case, there is not much difference between the results of Rossow using either 160 or 320 grid resolutions. According to Rossow, the results presented in Ref. [42] was not suitably described there. The results of Rossow presented in Fig. 7(b) were received directly from him. The comparison indicates that the accuracy of the current method is better than that of Rossow.

Inspecting the current solutions given in Figs. 3–7, it is observed that there are no oscillations around either shocks or discontinuities. Additionally, the solutions are very precise in the regions

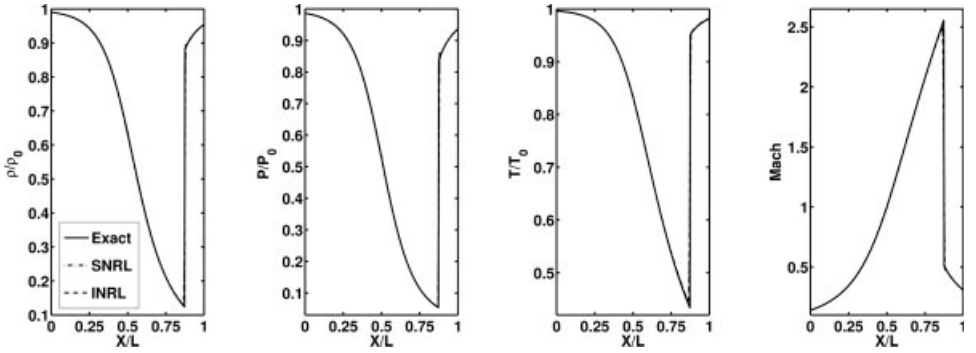

FIG. 6. The present results in a nozzle with $P_b = 45$ kPa using INRL and SNRL schemes and comparing them with the exact solutions.

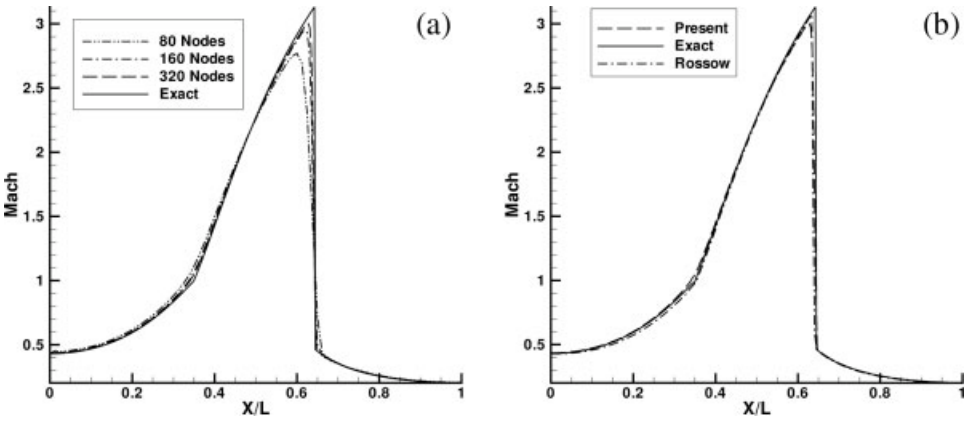

FIG. 7. Evaluating the current numerical solutions in solving the nozzle problem. (a) The grid refinement study. (b) Comparison with exact and Rossow [42] solutions.

with smooth to moderate variations. Back to the Computational Modelling section, we have not enforced any types of limiter, explicit damping function, explicit artificial viscosity, and so on in our formulations to damp out possible oscillations in our results. Despite excluding such key features, which are normally applied in shock-capturing methods, no major or minor oscillations are observed around discontinuities in our solutions.

B. Performance of the Two Linearization Schemes

Figure 8 presents the average number of iterations per time step κ to meet the specified convergence criterion at different Courant numbers. Figure 8(a) compares the performance of SNRL with that of INRL in shock tube problem. The problem is tested for both isentropic and isothermal conditions. We have tested the isothermal condition in order to eliminate the role of energy equation from the system of governing equations in our nonlinear iterations. As is expected, the

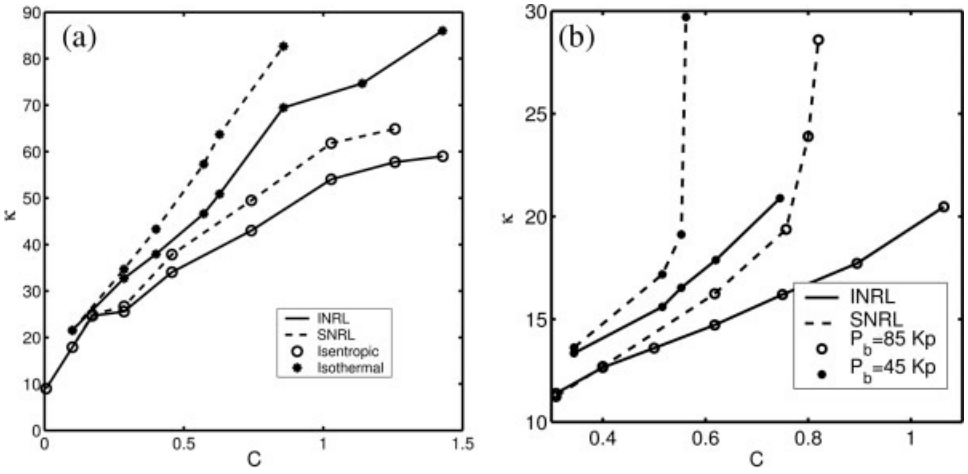

FIG. 8. The average number of iterations per time step versus Courant number. (a) The shock tube problem. (b) The nozzle problem.

average number of iterations per time step normally increases as Courant increases. Our experience showed that the number of iterations at earlier time steps would be much higher than the next ones. Additionally, the number of iterations may reduce to as low as 3–5 iterations per time step in Courant numbers less than 0.5 if time has elapsed enough. Irrespective of the type of two schemes, their performances show considerable difference as Courant increases. However, the differences diminish at lower Courant numbers. A careful comparison indicates that the choice of isothermal case results in a higher number of iterations with respect to the corresponding isentropic one. Therefore, the advantages of INRL with respect to SNRL are greater if the energy equation is coupled into the system of governing equations.

One important point shown in Fig. 8(a) is that the range of Courant number applicability is wider for INRL than that of SNRL in both isothermal and isentropic conditions. The difference is more pronounced in isothermal condition. As is seen, INRL converges to solution within a much wider range of Courant numbers at isothermal condition. The figure indicates that INRL converges to solutions for Courants close to 1.5 in isothermal condition; however, SNRL is restricted to a maximum Courant of about 0.85. Therefore, it is concluded that SNRL is more restricted to the range of large Courant number employment than INRL irrespective of employing either isentropic or isothermal conditions.

Figure 8(b) similarly compares the performance of SNRL with that of INRL in solving the nozzle problem with two back pressures of $P_b = 85$ and 45 kPa. Similar to the shock tube case, INRL generally exhibits greater performance than SNRL. In the other words, INRL scheme requires less number of iterations per time step to meet the convergence criterion at identical conditions. Comparing the results at the two chosen back pressures, it indicates that the method is more restricted to the range of large Courant employment as the back pressure decreases. It is because the normal shock standing in the divergent part becomes much stronger as P_b decreases. This effect is similarly observed using either INRL or SNRL schemes. However, SNRL is limited to lower Courants than INRL. As is seen, the number of iterations in case with $P_b = 45$ kPa drastically increases as Courant approaches 0.55. This ill performance is similarly observed when $P_b = 85$ kPa as Courant approaches 0.8. Contrary to SNRL, INRL does not perform such ill performances at the two back pressures. Additionally, its range of large Courant employment is much wider than SNRL.

Figures 8 compares the performance of INRL with that of SNRL at different conditions and a wide range of Courant numbers. However, it does not quantify the increase in performance. To quantify the qualitative progresses shown in this figure, the percentage reduction in the number of iterations per time step is defined as

$$\zeta = 100 \times (\kappa_{\mathrm{SNRL}} - \kappa_{\mathrm{INRL}})/\kappa_{\mathrm{INRL}} \tag{5.2}$$

where κ represents the average number of iterations per time step as illustrated in Fig. 8. Figure 9(a) demonstrates the percentage reduction versus Courant number. Moreover, Fig. 9(a) presents the results in solving the shock tube problem with either isentropic or isothermal conditions. As is observed, the percentage reduction behavior changes as Courant increases. It performs a decrease following a sharp increase. As is seen, the increase in performance is much more pronounced at the isothermal condition than the isentropic one. Indeed, the impact of using INRL is to cause a greater improvement in the performance of the method irrespective of employing either isothermal or isentropic conditions. The improvements are as large as 26% and 15% for the isothermal and isentropic conditions, respectively.

Similar to Fig. 9(a), Fig. 9(b) demonstrates the achieved improvement in solving the nozzle problem. The results are presented for two back pressures of 85 and 45 kPa. Indeed, this figure

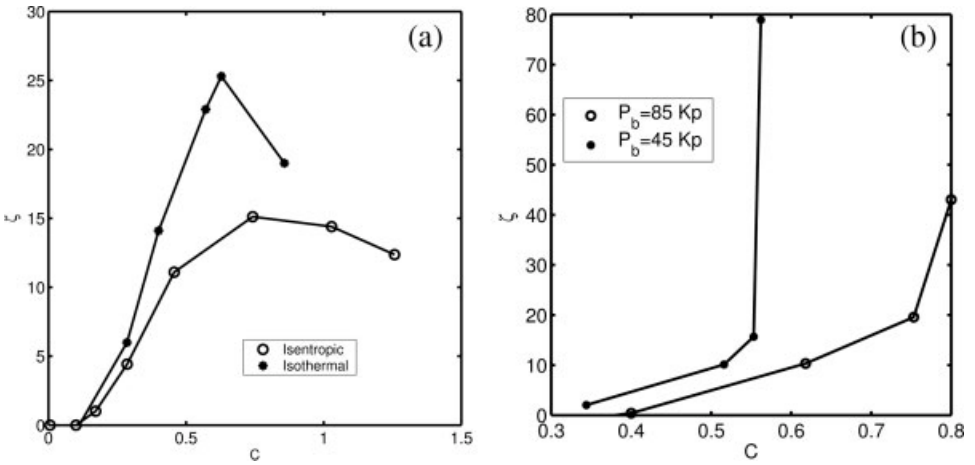

FIG. 9. The percentage reduction in the number of iterations versus Courant number. (a) The shock tube problem. (b) The nozzle problem.

quantifies the improvement illustrated in Fig. 8(b). As is observed, the improvement is excellent at both back pressures. Figure shows that INRL performs considerably better than SNRL in treating the steady compressible flow problem with shock, where a strong discontinuity stands in the domain. The figure also indicates that the performance will be boosted up drastically if the normal shock standing in the divergent part becomes stronger. In another words, the improvement in performance of INRL is considerable at lower back pressures. The improvement is dramatic as Courant approaches the limiting Courants. The improvements become as large as 42% and 80% for the cases with the weak and strong normal shocks, respectively.

To focus on a specific Courant number in solving the shock tube problem and quantify the improvement in the performance, Fig. 10 presents the results for a shock tube with various diaphragm pressure-ratios. Indeed, this study enables us to evaluate the performance of INRL

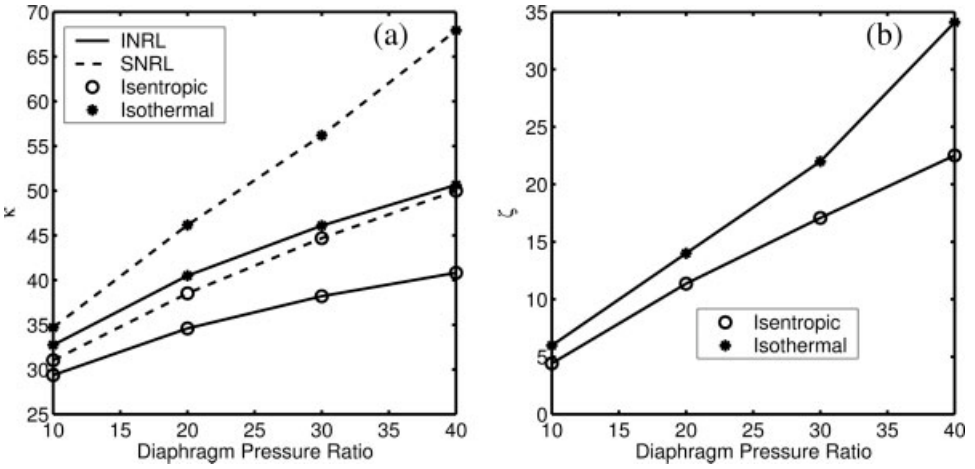

FIG. 10. The performance of INRL with respect to SNRL in solving the shock tube problem considering different diaphragm pressure ratios, C = 0.286. (a) Average number of iterations per time step. (b) Percentage reduction in number of iterations.

TABLE I. Improvement in the performance of the current collocated shock-capturing method using INRL scheme.

Test case	$\zeta_{max}\%$	$\eta\%$
Shock tube, isothermal, $r_p = 10.0$	26	70
Shock tube, isentropic, $r_p = 10.0$	15	14
Shock tube, isothermal, $r_p = 40.0$	23	N.A.
Shock tube, isentropic, $r_p = 40.0$	34	N.A.
Nozzle, $P_b = 85.0$ KPa	42	47
Nozzle, $P_b = 45.0$ KPa	80	67

in treating unsteady problems with stronger discontinuities. Figure 10(a) illustrates the average number of iterations per time step required to converge to the specified ϵ at $C = 0.286$. The results are for both isothermal and isentropic conditions. The problem has been solved for different diaphragm pressure ratios from $r_p = 10$ to 40. The moving shock, expansion waves, and discontinuity become much stronger in the shock tube if r_p increases. Figure 10(a) indicates that the performance of INRL increases as r_p increases. The improvement is similarly observed for both isentropic and isothermal conditions. It is concluded that the performance of INRL is not deteriorated as the discontinuities become stronger in the domain. Figure 10(b) quantifies the performances shown in Fig. 10(a). It presents the percentage reduction in the number of iterations per time step versus the diaphragm pressure ratio. As is observed, the improvement increases as the pressure-ratio increases. The improvements are as large as 34% in isothermal and 23% in isentropic conditions.

Table I summarizes the outcomes achieved in this section. Indeed, it presents the maximum percentage of improvement achieved by employing INRL scheme instead of the primitive SNRL one. The table is limited to a few cases, which were studied and discussed in this section. It provides two types of performances. The first one is the maximum percentage reduction in the number of iterations per time step ζ_{max}. The second one is the progress in the range of large Courant number applicability, which is defined as $\eta\% = 100 \times (C_{INRL} - C_{SNRL})/C_{SNRL}$. The table generally indicates that the improvements in the two evaluated parameters are great if INRL scheme is used in the collocated shock-capturing methods to solve both the stationary and non-stationary problems. The table also indicates that the performance of INRL with respect to SNRL increases as the discontinuities in the domain become stronger.

VI. CONCLUSION

A fully conceptual linearization strategy was suitably developed to linearize the convection terms in the momentum equations. The essence of strategy returns to the use of dual velocity definitions at the cell faces in finite-volume-based collocated-grid methods. The conceptual linearization maintains the original characteristics of the two velocities, which inevitably appear in the conservative statements of the governing equations. The results show that there will be considerable improvement in the performance of the primitive finite volume method if the conceptual meaning is fully authenticated in the linearization. Indeed, a wider range of large Courant number applicability in addition to benefit from a fewer number of iterations indicate that the conceptual linearization performs numerously better than the primitive linearization strategy. The conclusion was shown for both steady and transient flow problems. The current investigation showed that the improvement in the efficiency would be as large as 80%. This performance can still increase if the discontinuities in the domain become stronger. The current results also indicate that the solution is accurate

enough in the regions with smooth to moderate variations and it is non-oscillatory in the regions with discontinuities. This outcome is achieved without utilizing any types of numerical stabilizers such as explicit artificial viscosity, explicit damping functions, and limiters. The conceptual linearization does not deteriorate the accuracy at all. The advantages of the current linearization strategy can be equally reachable in the other finite-volume pressure-based collocated methods.

References

1. S. K. Godunov, A difference scheme for numerical computation of discontinuous solutions of fluid dynamics, Mat Sb 47 (1959), 271–306.
2. P. L. Roe, Approximate Riemann solvers, parameter vectors, and difference schemes, J Comput Phys 43 (1981), 357–372.
3. A. Harten, P. D. Lax, and B. Van Leer, On upstream differencing and Godunov-type schemes for hyperbolic conservation laws, SIAM Rev 25 (1983), 35–61.
4. A. C. Berkenbosch, E. F. Kaasschieter, and J. H. M. Thije Boonkkamp, Finite-difference methods for one-dimensional hyperbolic conservation laws, Numer Methods Partial Differential Equations 10 (1994), 225–269.
5. E. F. Toro, Riemann solvers and numerical methods for fluid dynamics, 2nd ed., Springer, Berlin, 1999.
6. V. Guinot, High resolution Godunov-type schemes with small stencils, Int J Numer Meth Fluids 44 (2004), 1045–1162.
7. D. Choi and C. L. Merkle, Application of time-iterative schemes to incompressible flow, AIAA J 23 (1985), 1518–1524.
8. R. Klein, Semi-implicit extension of a Godunov-type scheme based on low Mach number asymptotics I: One-dimensional flow, J Comput Phys (1995), 213–237.
9. R. Codina, M. Vazquez, and O. C. Zienkiewicz, A general algorithm for compressible and incompressible flows. III. The semi-implicit form, Int J Numer Methods Fluids 27 (1998), 13–32.
10. K. C. Karki and S. V. Patankar, Pressure based calculation procedure for viscous flows at all speeds in arbitrary configurations, AIAA J 27 (1989), 1167–1173.
11. F. S. Lien, A pressure-based unstructured grid method for all-speed flows, Int J Numer Methods Fluids 33 (2000), 355–374.
12. M. Darbandi and S. F. Hosseinizadeh, General pressure-correction strategy to include density variation in incompressible algorithms, J Thermophysics Heat Transfer 17 (2003), 372–380.
13. D. R. van der Heul, C. Vuik, and P. Wesseling, A conservative pressure-correction method for flow at all speeds, Comput Fluids 32 (2003), 1113–1132.
14. S. F. Hosseinizadeh and M. Darbandi, A quasi-one-dimensional pressure-based solution for subsonic Euler flow regime, Far East J Appl Math 21 (2005), 157–171.
15. C. C. Rossow, A blended pressure/density based method for the computation of incompressible and compressible flows, J Comput Phys 185 (2003), 375–398.
16. S. V. Patankar and D. B. Spalding, A calculation procedure for heat, mass, and momentum transfer in three-dimensional parabolic flows, Int J Heat Mass Transfer 15 (1972), 1787–1806.
17. H. K. Versteeg and W. Malalasekera, An introduction to computational fluid dynamics; the finite volume method, Longman Scientific and Technical, Harlow, Essex, UK, 1995.
18. S. Thangam and D. D. Knight, A computational scheme in generalized coordinates for viscous incompressible flows, Computers Fluids 18 (1990), 317–327.
19. H. Bijl and P. Wesseling, A unified method for computing compressible and incompressible flows in boundary-fitted coordinates, J Comput Phys 141 (1998), 153–173.

20. M. Zijlema, A. Segal, and P. Wesseling, Invariant discretization of $k - \epsilon$ model in general co-ordinate for prediction of turbulent flow in complicated geometries, Comput Fluids 24 (1995), 209–225.

21. M. Darbandi and M. Zakyani, Solving turbulent flow in curvilinear coordinate system using covariant velocity calculation procedure, G. R. Liu, V. B. C. Tan, and X. Han, editors, Computational Methods, Springer, The Netherlands, 2006, pp. 161–175.

22. S. Faure, Stability of a colocated finite volume scheme for the Navier–Stokes equations, Numer Methods Partial Differential Equations 21 (2004), 242–271.

23. C. M. Rhie and W. L. Chow, Numerical study of the turbulent flow past an airfoil with trailing edge separation, AIAA J 21 (1983), 1525–1532.

24. T. F. Miller and F. W. Schmidt, Use of a pressure-weighted interpolation method for the solution of the incompressible Navier–Stokes equations on a nonstaggered grid system, Numerical Heat Transfer 14 (1988), 213–233.

25. H. Askoy and C. J. Chen, Numerical solution of Navier–Stokes equations with nonstaggered grids using finite analytic method, Numerical Heat Transfer B 21 (1992), 287–306.

26. M. M. Rahman, A. Miettinen, and T. Siikonen, Modified SIMPLE formulation on a collocated grid with an assessment of the simplified QUICK scheme, Numerical Heat Transfer B 30 (1996), 291–314.

27. A. W. Date, Complete pressure correction algorithm for solution of incompressible Navier–Stokes equations on a nonstaggered grid, Numerical Heat Transfer B 29 (1996), 441–458.

28. M. Darbandi and G. E. Schneider, Analogy-based method for solving compressible and incompressible flows, J of Thermophysics and heat Transfer 12 (1998), 239–247.

29. M. Darbandi and S. F. Hosseinizadeh, A two-step modification toward implementing compressible source terms in low compressible flows, J Aerospace Science Technology 2 (2005), 37–44.

30. H. Paillère, P. Le Quèrè, C. Weisman, J. Vierendeels, E. Dick, M. Braack, F. Dabbene, A. Beccantini, E. Studer, T. Kloczko, C. Corre, V. Heuveline, M. Darbandi, and S. F. Hosseinizadeh, Modelling of natural convection flows with large temperature differences: A benchmark problem for low mach number solvers, Part 2: ESAIM: Mathematical Modelling and Numerical Analysis 39 (2005), 617–621.

31. M. Darbandi and S. F. Hosseinizadeh, Numerical simulation of thermobuoyant flow with large temperature variation, J Thermophys Heat Transfer 20 (2006), 285–296.

32. J. P. Van Doormal, G. D. Raithby, and B. H. McDonald, The segregated approach to predicting viscous compressible fluid flows, J Turbomachinery 109 (1987), 268–277.

33. J. C. Tannehill, R. S. Pletcher, and D. A. Anderson, Computational fluid mechanics and heat transfer, Taylor and Francis, Washington, 1997.

34. R. I. Issa, Solution of the implicitly discretized fluid flow equations by operator-splitting, J Comput Phys 62 (1986), 40–65.

35. R. I. Issa and M. H. Javareshkian, Pressure-based compressible calculation method utilizing total variation diminishing schemes, AIAA J 36 (1998), 1652–1657.

36. N. W. Bressloff, A parallel pressure implicit splitting of operators algorithm applied to flows at all speeds, Int J Numer Methods Fluids 36 (2001), 497–617.

37. M. Darbandi and G. E. Schneider, Momentum variable procedure for solving compressible and incompressible flows, AIAA J 35 (1997), 1801–1805.

38. M. Darbandi and G. E. Schneider, Comparison of pressure-based velocity and momentum procedures for shock tube problem, Numerical Heat Transfer B 33 (1998), 287–300.

39. M. Darbandi and G. E. Schneider, Performance of an analogy-based all-speed procedure without any explicit damping, Comput Mech 26 (2000), 459–469.

40. S. F. Wornom and M. M. Hafez, Implicit conservative schemes for the Euler equations, AIAA J 24 (1986), 215–223.

41. D. A. Venditti and D. L. Darmofal, Adjoint error estimation and grid adaption for functional outputs: application to quasi-one-dimensional flow, J Comput Phys 164 (2000), 204–227.

42. C. C. Rossow, Extension of a compressible code toward the incompressible limit, AIAA J 41 (2003), 2379–2386.

43. J. Y. Yang, F. S. Lien, and C. A. Hsu, Non-oscillatory shock capturing finite element methods for the one-dimensional compressible Euler equations, Int J Numer Methods Fluids 11 (1990), 405–426.

44. M. Darbandi and S. M. Bostandoost, A new formulation toward unifying the velocity role in collocated variable arrangement, Numerical Heat Transfer B 47 (2005), 361–382.

45. M. Darbandi and V. Mokarizadeh, A modified pressure-based algorithm to solve the flow fields with shock and expansion waves, Numerical Heat Transfer B 46 (2004), 497–504.

46. C. Prakash and S. V. Patankar, A control volume-based finite-element method for solving the Navier–Stokes equations, using equal-order velocity-pressure interpolation, Numerical Heat Transfer 8 (1985), 259–280.

47. G. E. Schneider and M. J. Raw, Control volume finite element method for heat transfer and fluid flow using co-located variables - 1.Computational procedure, Numerical Heat Transfer 11 (1987), 363–390.

48. M. Sun and K. Takayama, An artificially upstream flux vector splitting scheme for the Euler equations, J Comput Phys 189 (2003), 305–329.

49. V. A. Titarev and E. F. Toro, WENO schemes based on upwind and centered TVD fluxes, Comput Fluids 34 (2005), 705–720.